

# Semantic-ICP: Iterative Closest Point for Non-rigid Multi-Organ Point Cloud Registration

Wanwen Chen<sup>a</sup>, Qi Zeng<sup>a</sup>, Carson Studders<sup>b</sup>, Jamie J.Y. Kwon<sup>b</sup>, Emily H.T. Pang<sup>b</sup>, Eitan Prisman<sup>b</sup>, Septimiu E. Salcudean<sup>a</sup>

<sup>a</sup>*Department of Electrical and Computer Engineering, University of British Columbia, 2332 Main Mall, Vancouver, V6T 1Z4, BC, Canada*

<sup>b</sup>*Faculty of Medicine, University of British Columbia, 317 – 2194 Health Sciences Mall, Vancouver, V6T 1Z3, BC, Canada*

---

## Abstract

Point cloud registration is important in computer-aided interventions (CAI). While learning-based point cloud registration methods have been developed, their clinical application is hampered by issues of generalizability and explainability. Therefore, classical point cloud registration methods, including Iterative Closest Point (ICP), are still widely applied in CAI. ICP methods fail to consider that: (1) the points have well-defined semantic meaning, in that each point can be related to a specific anatomical label; (2) the deformation required for registration needs to follow biomechanical energy constraints. In this paper, we present a novel non-rigid semantic ICP (SemICP) method that handles multiple point labels and uses linear elastic energy regularization. We use semantic labels to improve the robustness of closest point matching and propose a novel point cloud deformation representation that incorporates explicit biomechanical energy regularization. Our experiments on four datasets show that our method significantly improves the Hausdorff distance and mean surface distance compared with other point cloud registration methods. We also demonstrate that integrating deep learning segmentation models with our registration pipeline enables effective alignment of US and MR point clouds.

---

\*The work is supported by an NSERC Discovery Grant and the Charles Laszlo Chair in Biomedical Engineering held by Dr. Salcudean, the VCHRI Innovation and Translational Research Awards, the University of British Columbia Department of Surgery Seed Grant and CIHR Project Grant held by Dr. Prisman.

*Email address:* wanwenc@ece.ubc.ca (Wanwen Chen)

*Keywords:*

Point cloud registration, Iterative Closest Point, Elastic Energy Regularization.

---

## 1. Introduction

Registration is an important problem in computer-aided intervention (CAI). To enhance visualization of surgical planning, CAI systems require registration of preoperative volumes to intraoperative volumes, meshes, or surfaces. Point clouds represent critical anatomical structures as spatial points, providing a modality-agnostic, sparse and flexible representation. In particular, in ultrasound (US) to cross-sectional image registration problems, US typically provides only partial observations of internal structures, making volume-based registration challenging. Moreover, bone surfaces and other highly reflective structures in US cause acoustic shadows and incomplete volumes. As a result, converting segmented images to point clouds has become a common and effective approach for US registration in US-guided CAI systems (Lei et al. (2023); Jiang et al. (2025); Hiep et al. (2025)).

Deep learning models have emerged in point cloud registration (Wang and Solomon (2019); Poiesi and Boscaini (2022)), but they are data-hungry and struggle to generalize to different tasks. Indeed, a recent study shows that a deep learning model trained on general point clouds cannot be applied to CT patient registration out-of-the-box and has lower performance compared with RANSAC initialization and ICP refinement (Weber et al. (2024)). In general, fine-tuning deep learning models on specific datasets is required to achieve adequate performance (Zhang et al. (2024)). However, this is rarely feasible due to the limited training data in a specific CAI application. Furthermore, deep learning models often lack the explainability required for clinicians to trust their application in medical interventions. Therefore, a generalizable and explainable optimization-based point cloud registration is preferable in CAI.

One of the most representative optimization-based registration algorithms, Iterative Closest Point (ICP) (Besl and McKay (1992)), is widely used in CAI (Ma et al. (2023)) and has been applied in recent navigation systems for spine surgery (Liebmann et al. (2024)) and oral and maxillofacial surgery (Bayrak et al. (2020)). However, the semantic information of the point cloud, such as the points' anatomical labels, is not utilized in the original ICP. Furthermore, most registration tasks in medical imaging involve soft tissue, requiring

non-rigid ICP-based registration. Prior methods deal with deformation by locally affine regularization, ignoring the underlying biomechanical effects (Amberg et al. (2007); Yao et al. (2020, 2023)). Addressing these problems, we propose and validate a novel non-rigid ICP registration method that utilizes the semantic information and introduces explicit linear biomechanical energy regularization.

### *1.1. Related Work*

#### *1.1.1. ICP and its Variants*

ICP (Besl and McKay (1992)) was developed over 30 years ago, but it is still widely applied in medical point cloud registration for CAI. ICP iteratively finds the closest point pairs in two point clouds, and the corresponding point pairs are used to estimate a rigid transformation to move the source point cloud closer to the target point cloud. The initial alignment between the two point clouds should be close enough to ensure convergence, making the original ICP algorithm sensitive to initialization and outliers and less effective due to local minima. To alleviate these problems, Global-ICP (Yang et al. (2015)) performs a global search over 3D space. Fast-robust-ICP (Zhang et al. (2022)) uses Welsch’s function to improve the robustness of the error metric. However, the above ICP methods estimate only rigid transformations. Therefore, their utility is limited to medical applications in which tissue deformation is negligible.

To address non-rigid registration, non-rigid ICP (Amberg et al. (2007)) extends ICP to estimate the surface deformation using a similar nearest-point search to find the point correspondences. The deformation is regularized using a local affine transformation. It has been used in US-guided augmented reality navigation for liver procedures (Ma et al. (2022)). More recent non-rigid ICP registration methods focus on accelerating convergence and increasing robustness. Yao et al. (2020) use a deformation graph with a globally smooth robust estimator to regularize the deformation, and then use accelerated optimization to improve the runtime (Yao et al. (2023)). However, these methods are not regularized by physical parameters; they only consider local affine regularization, which cannot capture the underlying biomechanical characteristics within medical point clouds.

#### *1.1.2. Semantic-assisted Point Cloud Registration*

To our best knowledge, incorporating semantic segmentation in point matching for ICP has only been presented in the context of rigid registration

in autonomous driving, showing improved accuracy compared with regular ICP. Zaganidis et al. (2018) use PointNet to segment light detection and ranging (LiDAR) point clouds and use the segmentation to aid point matching. Wang et al. (2020) segment the LiDAR point cloud to cars or the background before performing ICP. For medical applications, we became aware of concurrent work published after our preprint (Flepp et al. (2025)) that integrates point label-informed matching in bone CT-X-ray rigid registration. However, their work is limited to rigid registration and therefore cannot account for surface deformation, which is critical in medical point cloud registration. Our approach remains distinct in its focus on non-rigid registration and in providing a more systematic evaluation across four datasets, whereas the concurrent work was evaluated on only one dataset. Previous work that utilized the semantic information of point labels performed registration on each anatomy separately. Hiep et al. (2025) segment bones and arteries from US and perform ICP registration on them separately. However, these studies do not account for interactions between organs or surrounding tissues, failing to capture their interdependent motion. Our method introduces a novel and practical control grid-based deformation representation to model inter-object interaction with a biomechanical energy-inspired regularizer in the point cloud registration step. Soft semantic-based matching that learns feature expressions of the point for point matching has also been proposed (Hansen et al. (2019); Mekhzoum et al. (2024)). However, the learned features can be difficult to generalize to different anatomies, while utilizing the consistency of the anatomical labels from the upstream tasks can be applied to any segmentation-generated point clouds, without requiring an anatomy-specific feature extraction step.

### *1.1.3. Biomechanics-inspired Regularization in Point Cloud Registration*

Previous work introducing biomechanical constraints into point cloud registration requires sophisticated finite element modeling (FEM). The regularization can be introduced through iterative FEM directly (Khallaghi et al. (2015); Ringel et al. (2023); Yang et al. (2025)), but FEM is time-consuming and computationally intensive. Data-driven biomechanical models implicitly introduce the constraints by learning from finite element simulation (Fu et al. (2021a,b); Wang et al. (2024)). However, these models have only been evaluated on the organs used for training, making it unclear whether they can generalize to other organs. Retraining the models for a new domain, on the other hand, requires generating simulated data with time-consuming FEM.

Physics or biomechanics-inspired regularization can improve physical plausibility, and it has been introduced through a discrete approximation to the continuous elastic energy in 3D voxels (Broit (1981); Fischer and Modersitzki (2008); Nir et al. (2013)). However, the challenge of introducing this regularization into point cloud registration is that the point clouds only represent the deformation field as surface point movement, which solely describes the boundary conditions of the deformation field. Recently, Heinrich et al. (2023, 2025) introduced novel regularization in point cloud registration by voxelizing the point clouds to a dense representation to stabilize deep learning-based point cloud registration. Compared with dense voxels, we propose to use control point-based deformation that works directly on the points to reduce the memory cost. Their work also does not consider explicit biomechanical energy regularization, which is necessary for medical point cloud registration.

### *1.2. Contributions*

In this paper, we propose a new point-matching-based registration method for medical point cloud registration that addresses the lack of semantic information and biomechanical energy regularization in ICP. Our method first extends the semantic label-informed point-matching to non-rigid medical point cloud registration to ensure semantic-consistent matching, and then introduces a novel deformation representation in point clouds, along with explicit biomechanical energy regularization, into point cloud registration. The method was tested on three different datasets and achieved the best surface matching performance compared with other baseline algorithms. It is also tested on an additional dataset to show its ability to be integrated with upstream learning-based labelers, achieving accurate point cloud alignment. Our contributions include: (1) systematically introducing semantic label consistent point matching for non-rigid point matching-based point cloud registration; (2) a novel control-point-based deformation representation in optimization-based point cloud registration that enables practical elastic regularization; (4) validation of the effectiveness of our method in medical point clouds, with a fixed set of hyperparameters that underwent minimal tuning.

The rest of this paper is organized as follows. Section 2 describes the proposed method, and Section 3 presents validation results on four datasets, ablation studies, and sensitivity analyses. Section 4 provides the discussion.

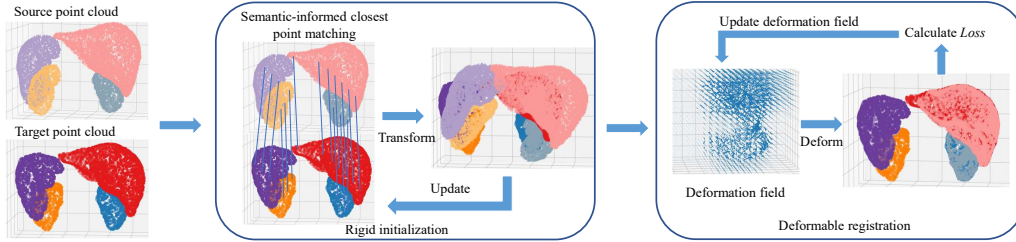


Figure 1: The workflow of our proposed Sem-ICP. The method includes a rigid initialization, and then the deformation is estimated iteratively.

## 2. Methods

We define the source point cloud as  $P = \{\mathbf{p}_0, \mathbf{p}_1, \dots, \mathbf{p}_N\}$  and the target as  $Q = \{\mathbf{q}_0, \mathbf{q}_1, \dots, \mathbf{q}_M\}$ , with the points  $\mathbf{p}, \mathbf{q} \in \mathbb{R}^3$ . The point clouds are associated with semantic labels  $L_p = \{x_0, x_1, \dots, x_N\}$  and  $L_q = \{y_0, y_1, \dots, y_M\}$ . The labels belong to the label set  $L = \{l_1, l_2, \dots, l_K\}$ , where  $K$  is the number of labels. We assume that the observed points have at least two labels,  $K \geq 2$ . Apart from the 3D location of the points, the point clouds also have local normals at each point:  $N_p = \{\mathbf{n}_0, \dots, \mathbf{n}_N\}$ ,  $N_q = \{\mathbf{m}_0, \dots, \mathbf{m}_M\}$ . The local normals can be estimated using surface reconstruction methods such as ball pivoting (Bernardini et al. (2002)). The registration workflow of Semantic-ICP (SemICP), is shown in Fig. 1; it first estimates a rigid transform  $\mathbf{T} \in SE(3)$ , then refines it by non-rigid registration.

### 2.1. Rigid Initialization

The optimal rigid transform  $\mathbf{T} \in SE(3)$  is iteratively estimated by minimizing a cost function that measures the difference between point clouds, as described in Algorithm 1. SemICP uses the semantic information during point pair matching, such that matched point pairs have the same semantic labels. At each iteration  $i$ , for each point  $\mathbf{p}_j$  from  $P$ , we find the closest point  $\mathbf{q}_j$  in  $Q$  that has the smallest L2 distance with the same semantic label as  $\mathbf{p}_j$ . KD-tree is used to accelerate the search for matched point pairs. The update value  $\Delta \mathbf{T}^i$  is automatically estimated using the autograd function in PyTorch. We use an Adam optimizer (Kingma and Ba (2014)) to minimize the cost function  $L_{rigid}$  that measures the point-to-plane distance (Segal et al.

(2009)) of matched point pairs at each iteration:

$$L_{rigid} = \sum_{j=1}^N |(\mathbf{R}\mathbf{p}_j^i + \mathbf{t} - \mathbf{q}_j^i) \cdot \mathbf{m}_j| , \quad (1)$$

$\mathbf{t}$  is the translation and  $\mathbf{R}$  is the rotation of the rigid transformation  $\mathbf{T}$  between the two point clouds.  $\mathbf{R}$  is parametrized by XYZ Euler angles.  $\mathbf{m}_j$  is the local normal of point  $\mathbf{p}_j$ , and the cost function measures the error along the surface normal. Compared with point-to-point L2 distance, point-to-plane distance encourages the matched points to be on the same plane instead of being strictly aligned. The matched point pairs are recomputed at each iteration with the updated source point cloud. The iteration is repeated until  $L_{rigid}$  is no longer improved or the maximum number of iterations is reached.

---

**Algorithm 1** Rigid initialization

---

**Input:** Source point cloud  $P$  and target point cloud  $Q$ .

**Output:** Optimal rigid transformation  $\mathbf{T}$ .

- 1: Initialization:  $\mathbf{T}^0 = \mathbf{I}, P^0 = P$ .
  - 2: **for**  $i = 0$  to  $max\_iter - 1$  **do**
  - 3:   **for**  $l \in L$  **do**
  - 4:     Point sets  $P_{sub}^i, Q_{sub}$  with the same label  $l$ .
  - 5:     **for**  $\mathbf{p}_j^i$  in  $P_{sub}^i$  **do**
  - 6:       Computed closest point  $\mathbf{q}_j^i$  with smallest L2 distance.
  - 7:     **end for**
  - 8:   **end for**
  - 9:    $\Delta\mathbf{T}^i \leftarrow \arg \min L_{rigid}(\mathbf{T}^i)$
  - 10:  $\mathbf{T}^{i+1} \leftarrow \Delta\mathbf{T}^i + \mathbf{T}^i, P^{i+1} \leftarrow \Delta\mathbf{T}^i P^i$
  - 11:   **if** Converge **then**
  - 12:     break
  - 13:   **end if**
  - 14: **end for**
  - 15: **return**  $\mathbf{T}^{final}$
- 

## 2.2. Non-rigid Registration

Non-rigid registration is performed after the initial rigid alignment. The non-rigid registration estimates the deformation field  $\mathbf{D}$  that deforms the

source point cloud  $P$  to be aligned with the target  $Q$ . Instead of parameterizing the deformation  $\mathbf{D}$  as the movement at each surface point  $\mathbf{p}$ , we uniformly sample  $N_C$  control points  $\mathbf{C} = \{\mathbf{c}_i = (x_1^i, x_2^i, x_3^i), i = 1, 2, \dots, N_C\}$  in the point cloud bounding box, and use the deformation  $\mathbf{d}_c$  at these control points to describe the deformation field  $\mathbf{D} \in \mathbb{R}^{N_C \times 3}$ , where  $\mathbf{D}(i) = \mathbf{d}_{c_i}$ . Our new point cloud deformation field representation provides several improvements over the state of the art. First, the control point-based representation is more consistent in memory usage since it does not depend on the density of the input point clouds. Second, the individual point movement is more regularized because it is interpolated from neighboring control points. Last but not least, this new deformation representation enables *explicit* biomechanics-based regularization, since it also models the inner tissue deformation rather than only describing the boundary conditions.

The deformation is iteratively estimated, as shown in Algorithm 2. In each iteration  $i$ , we use the same label-informed nearest point matching method employed earlier during rigid initialization to find the matched point pair  $(\mathbf{p}_j^i, \mathbf{q}_j^i)$ , and use the Adam optimizer to minimize the loss:

$$L_{non-rigid}(\mathbf{D}) = \sum_{j=1}^N \|\mathbf{p}_j^i + \mathbf{d}_j - \mathbf{q}_j^i\|_2 + Reg(\mathbf{D}) \quad (2)$$

$\mathbf{d}_j$  is the surface point deformation at point  $\mathbf{p}_j$ . We compute  $\mathbf{d}_j$  using a trilinear interpolation of the deformation at the control points that are in  $\mathbf{p}$ 's neighborhood. The neighborhood of a control point is defined as the 26 points connected with it.

$$\mathbf{d}_j = interpolate(\mathbf{d}_{\mathbf{c}_1}, \dots, \mathbf{d}_{\mathbf{c}_n}), \{\mathbf{c}_1, \dots, \mathbf{c}_n\} = Neighbor(\mathbf{p}_j) \quad (3)$$

The first term in (2) minimizes the distance between the matched point pairs, while the remaining regularization term controls tissue deformation. The regularization term includes elastic energy  $Reg_{els}$ , deformation magnitude  $Reg_{mag}$  and the smoothness of deformation field  $Reg_{grad}$ :

$$Reg(\mathbf{D}) = \alpha Reg_{els}(\mathbf{D}) + \beta Reg_{mag}(\mathbf{D}) + \gamma Reg_{grad}(\mathbf{D}) \quad (4)$$

We use linear elastic regularization (Fischer and Modersitzki (2004); Nir et al. (2013)) to regularize the deformation. In continuum mechanics, the linear elastic energy can be described using the Navier-Lamé Equation. We approximate the Navier-Lamé Equation with the numerical differentiation at

the control points and add a scaling factor to normalize the energy, where  $\Delta$  is the step size of the control points.

$$Reg_{els}(\mathbf{D}) = \frac{\Delta}{N_C} \sum_{\mathbf{c}} \left( \frac{\mu}{4} \sum_{j=1}^3 \sum_{k=1}^3 \left( \frac{\partial \mathbf{D}_j}{\partial x_k} + \frac{\partial \mathbf{D}_k}{\partial x_j} \right) + \frac{\lambda}{2} (\nabla \mathbf{D})^2 \right) \quad (5)$$

We use a two-point estimation for numerical differentiation:

$$\frac{\partial \mathbf{D}_i}{\partial x_j} = \frac{\mathbf{D}(x_j + \Delta, i) - \mathbf{D}(x_j, i)}{\Delta}, \quad \nabla \mathbf{D} = \sum_{i=1}^3 \frac{\partial \mathbf{D}_i}{\partial x_i} \quad (6)$$

$\lambda$  and  $\mu$  are Lamé parameters, which can be estimated based on Young’s modulus  $E$  and Poisson’s ratio  $\nu$ :

$$\lambda = \frac{E\nu}{(1+\nu)(1-2\nu)}, \quad \mu = \frac{E}{2(1+\nu)} \quad (7)$$

In addition to the above energy regularization, the regularization term also includes magnitude regularization  $Reg_{mag}$  to reduce unwanted large deformation at the control point  $\mathbf{c}_i$ , and a gradient regularization  $Reg_{grad}$  to encourage control grid smoothness:

$$Reg_{mag}(\mathbf{D}) = \frac{1}{N_C} \sum_i^{N_C} \|\mathbf{c}_i\|_2 \quad (8)$$

$$Reg_{grad}(\mathbf{D}) = \frac{\Delta}{N_C} \sum_{\mathbf{c}} \left\| \frac{\partial \mathbf{D}}{\partial x_1} \right\|_2 + \left\| \frac{\partial \mathbf{D}}{\partial x_2} \right\|_2 + \left\| \frac{\partial \mathbf{D}}{\partial x_3} \right\|_2 \quad (9)$$

### 3. Experiments and Results

#### 3.1. Datasets

The experiments are performed on one private dataset derived from transoral robotic surgery (TORS), and two public datasets from Learn2Reg challenges (Hering et al. (2022)). We use the training data in the Learn2Reg challenges, since label maps for test data are not included in the public

---

**Algorithm 2** Non-rigid refinement

---

**Input:** Source point cloud  $P$  and target point cloud  $Q$ .

**Output:** Optimal deformation field  $D$ .

```
1: Initialization:  $D^0 = \mathbf{0}$ .
2: for  $i = 0$  to  $max\_iter - 1$  do
3:   for  $j \in N$  do
4:      $d_j^i = interp(D^i)$  at  $p_j$ ,  $p_j^i = p_j + d_j^i$ 
5:   end for
6:   Find point pairs  $(p_j^i, q_j^i)$  (line 3-8 in Algorithm 1)
7:    $\Delta D^i \leftarrow \arg \min L_{non-rigid}(D^i)$ 
8:    $D^{i+1} \leftarrow \Delta D^i + D^i$ 
9:   if Converge then
10:    break
11:   end if
12: end for
13: return  $D^{final}$ 
```

---

dataset link<sup>1</sup>. We also utilize an additional private liver MR-3D US dataset that incorporates learning-based point cloud labeling and elastography for tissue stiffness measurement. 3D slicer is used to extract point clouds from the label maps (Fedorov et al. (2012)).

**TORS:** This dataset contains 3D freehand US and CT images of the neck collected from patients who underwent TORS for oral cancer between January 2022 and November 2024 at the Vancouver General Hospital (Vancouver, BC, Canada). This study received ethics approval from the University of British Columbia Clinical Research Ethics Board (H19-04025). Informed consent was obtained from all participants included in this study. Diagnostic CT data were collected preoperatively, and US data were collected before surgery while patients were anesthetized. A BK3500 with a 14L3 linear 2D transducer (BK Medical, Burlington, MA) and a Polaris Spectra (Northern Digital, ON, Canada) were used to collect freehand 3D US. PLUS (Lasso et al. (2014)) was used to calibrate the US probe and collect tracked US data. The image depth was set to 4 or 5 cm (depending on patient anatomy) at 9 MHz, and US imaging was carried out ipsilateral to the tumor. A medical student and an experienced research assistant labeled the carotid artery,

---

<sup>1</sup><https://learn2reg.grand-challenge.org/Datasets/>

jugular vein, and larynx/mandibular bone in 2D US frames and CT volumes, then the 2D US label maps were reconstructed in 3D. The dataset contains 24 pairs of US-CT images from 12 patients. The bifurcation point and the axis of the carotid in US and CT were used to pre-align volumes.

**AbdominalMRCT** (Clark et al. (2013)): The Learn2reg dataset contains 8 pairs of intra-patient abdominal magnetic resonance (MR) and CT images. The label maps include 3D segmentation of 4 anatomical labels of liver, spleen, right kidney and left kidney.

**HippocampusMR** (Simpson et al. (2019)): The Learn2reg challenge dataset includes MR images from 90 healthy adults and 105 adults with a non-affective psychotic disorder, along with segmentations of the head and body of the hippocampus. We use the validation registration pairs provided in the dataset’s JSON files, resulting in 60 inter-patient registration pairs.

**LiverMR-3DUS** (Zeng et al. (2021, 2024)): The private MR-3DUS dataset was collected from an earlier liver vibro-elastography imaging validation study with the approval of the UBC Clinical Research Ethics Board (H14-01964). The dataset contains intra-subject MR and 3D US image data from 19 healthy subjects and 20 patients with chronic liver diseases. Each subject completed MR exams with Achieva 3T or Ingenia Elition 3T X scanners (Philips Healthcare, Best, Netherlands). The abnormal image volumes were used with a voxel size of  $0.9375 \text{ mm} \times 0.9375 \text{ mm} \times 1.5 \text{ mm}$ . The US exam used a 3D B-mode acquisition with the EPIQ 7G system and the X6-1 xMATRIX array transducer (Philips Healthcare, Bothell, WA), with a 16 cm imaging depth and a  $90^\circ$  (lateral)  $\times 60^\circ$  (elevational) field of view, repeated 5 to 8 times. The voxel size for 3D US volumes was  $0.468 \text{ mm} \times 0.3231 \text{ mm} \times 0.6731 \text{ mm}$ . The dataset contains 174 MR-3D US image pairs. Gallbladder, inferior vena cava (IVC), right kidney, and major hepatic vessel branches were manually segmented by experts as registration surrogates.

### 3.2. Compared Baselines

We compare our method with different types of established point cloud registration methods. The first type of methods are rigid and non-rigid point-matching-based point cloud registration, which are the most similar methods to our method. The baseline methods include: the original ICP (Besl and McKay (1992)), Global-ICP (GO-ICP) (Yang et al. (2015)), Fast-robust-ICP (FR-ICP) (Zhang et al. (2022)), non-rigid ICP (NR-ICP) (Amberg et al. (2007)), Fast-RNRR (Yao et al. (2020)), AMM-NRR (Yao et al. (2023)). The second type of method is probabilistic-based registration, and we choose

to use Coherent Point Drift (CPD) (Gatti and Khallaghi (2022)) to provide a GMM-based point cloud registration baseline. To compare with learning-based methods, we choose to use the two Deep Closest Point (DCP) models described in (Wang and Solomon (2019)) trained on ModelNet40 (Wu et al. (2015)). DCPv1 uses a Dynamic Graph CNN as the embedding model to learn the feature representation of the points, and performs matching on the features directly, while DCPv2 introduces a transformer block for the point matching. We used the default parameters provided in the open-source codes of the baselines. For ICP, GO-ICP, and CPD, we downsample the point cloud to 1000 points to accelerate their run time. For DCP, we follow the paper’s implementation, downsampling the point cloud to 1024 points, and normalizing them to a uniform ball.

To evaluate the point cloud surface similarity, we use the 95th percentile of the Hausdorff Distance (HD95) and the mean surface distance (MSD) to determine the surface differences between the source and target point clouds.

$$HD95(P, Q) = \text{Percentile}_{95} \sum_{\mathbf{p} \in P} (\min_{\mathbf{q} \in Q} \|\mathbf{p} - \mathbf{q}\|_2) \quad (10)$$

$$MSD(P, Q) = \frac{1}{N_p} \sum_{\mathbf{p} \in P} (\min_{\mathbf{q} \in Q} \|\mathbf{p} - \mathbf{q}\|_2) \quad (11)$$

In the synthetic sensitivity study, we also report the average target registration error (TRE).

$$TRE(P, Q) = \frac{1}{N_p} \sum_{\mathbf{p} \in P} \|\mathbf{p} - \mathbf{q}\|_2 \quad (12)$$

To evaluate the deformation field’s topology, we report the standard deviation of the logarithmic Jacobian determinant (SDLogJ) that measures spatial distortion.

### 3.3. Implementation Details

The methods were implemented with a 12GB Nvidia GeForce RTX 3060 GPU, using Python 3.9.18, PyTorch 2.1.2, and CUDA-11.8. In the rigid initialization, the point clouds are downsampled to 1000 points, and the learning rate of the optimizer is 0.001 and the maximum number of iterations is 500. For non-rigid refinement, the learning rate is 0.01, and the maximum number of iterations is 300. The optimization will be stopped early when the loss is no longer improved. Each point’s coordinate was normalized to [-1,1] for better convergence, and we uniformly sampled  $25 \times 25 \times$

25 control points in the  $[-1, 1]^3$  space. The resulting spacing of the control grids for three datasets are: 2.04 mm $\times$ 2.43 mm $\times$ 3.66 mm for TORS dataset, 12.78 mm $\times$ 8.88 mm $\times$ 10.03 mm for AbdominalMRCT dataset, 0.97 mm $\times$ 1.69 mm $\times$ 1.11 mm for HippocampusMR dataset. We assume that all the tissues have a Young’s modulus of  $E = 1\text{kPa}$  (Chen et al. (1996)) and are almost incompressible, with a Poisson’s ratio of  $\nu = 0.499$ . The codes will be made public, accompanying the published paper.

### 3.4. Evaluation on Datasets

We report the quantitative evaluation using HD95 and MSD across three datasets, as shown in Tables 1 to 3. Compared to other baselines, our method SemICP achieves the lowest HD95 and MSD for each anatomical structure, as well as the lowest average across labels, on all three datasets.

**TORS:** The quantitative results are shown in Table 1. AMM-NRR and Fast-RNRR completed registration on only 7 pairs of 24 data pairs, with numerical issues affecting the remaining data. One Fast-RNRR result was highly inaccurate and is treated as a failed registration, not included in the final analysis. One unique challenge associated with this dataset is that the US provides only partial observation of relevant anatomical structures, especially the larynx and bony structures, resulting in differing point cloud sizes between US and CT. Additionally, visibility varies across anatomical structures. Our results show that other registration methods have larger HD95 and MSD when registering all anatomical structures, especially the larynx and bony structures. Without semantic information, other non-rigid registration algorithms under-penalize the larynx/bone registration error. Mismatching different structures also occurs in other baselines without semantic information, as shown in the qualitative evaluation in Fig. 2. Our method improves the delineation of anatomical structures and leads to significantly lower HD95 and MSD across all labels, greatly improving registration accuracy. It is worth noted that deep learning-based methods, DCPv1 and DCPv2, increases the surface matching error, showing that these models can not be applied in an out-of-box manner for TORS dataset. Our method also performs registration faster than other non-rigid registration methods, with an average computation time as 34.51 seconds, showing the potential to be utilized in image guidance systems to perform registration.

**AbdominalMRCT:** Table 2 show and HD95 and MSD on this dataset. Results for AMM-NRR and Fast-RNRR are reported on only 7 MR-CT pairs due to a numerical problem encountered with one point cloud pair. The

Table 1: The average HD95 on the TORS dataset. The metrics are reported in mean (std) in *mm* and the best performance is highlighted in bold.

	HD95				MSD				Runtime
	Carotid	Larynx/bone	Vein	Average	Carotid	Larynx/bone	Vein	Average	
Initial	5.47 ± 2.68	10.21 ± 9.27	10.85 ± 4.29	8.84	2.19 ± 0.92	4.72 ± 4.26	5.25 ± 2.52	4.05	
ICP	6.22 ± 2.99	7.07 ± 10.11	5.41 ± 2.99	6.24	2.47 ± 1.25	2.95 ± 5.59	2.32 ± 1.39	2.58	<b>0.04 ± 0.01</b>
GO-ICP	6.22 ± 3.56	5.53 ± 8.21	5.06 ± 2.35	5.60	2.44 ± 1.29	1.73 ± 2.26	2.22 ± 1.04	2.13	6.85 ± 1.37
FR-ICP	7.84 ± 4.95	7.78 ± 8.92	7.17 ± 5.69	7.60	2.87 ± 1.83	3.40 ± 5.68	2.93 ± 2.31	3.07	189.11 ± 95.49
CPD	10.70 ± 2.86	9.48 ± 7.43	8.87 ± 6.65	9.68	4.47 ± 1.17	3.67 ± 3.22	3.86 ± 3.72	4.00	2.78 ± 0.85
DCPv1	27.32 ± 8.30	15.53 ± 9.01	26.58 ± 13.70	23.14	12.97 ± 4.84	9.49 ± 6.91	15.59 ± 10.76	12.36	0.14 ± 0.40
DCPv2	25.63 ± 7.60	15.52 ± 9.49	25.62 ± 13.53	22.25	12.02 ± 4.45	9.45 ± 7.73	14.22 ± 11.08	11.89	0.15 ± 0.40
nr-ICP	8.27 ± 5.25	5.90 ± 9.41	5.98 ± 5.44	6.72	3.38 ± 2.52	2.54 ± 5.36	2.66 ± 2.73	2.86	165.49 ± 243.38
AMM-NRR	17.4 ± 0.40	4.10 ± 3.24	3.08 ± 0.72	2.97	0.71 ± 0.10	1.70 ± 2.16	0.93 ± 0.12	1.11	894.98 ± 188.62
Fast-RNRR	3.01 ± 1.58	5.92 ± 5.08	6.53 ± 5.12	5.15	1.25 ± 0.66	2.74 ± 3.34	3.09 ± 2.44	2.36	2408.30 ± 3755.40
SemICP	<b>0.63 ± 0.18</b>	<b>1.17 ± 2.33</b>	<b>0.69 ± 0.40</b>	<b>0.83</b>	<b>0.31 ± 0.05</b>	<b>0.36 ± 0.35</b>	<b>0.32 ± 0.10</b>	<b>0.33</b>	34.51 ± 16.96

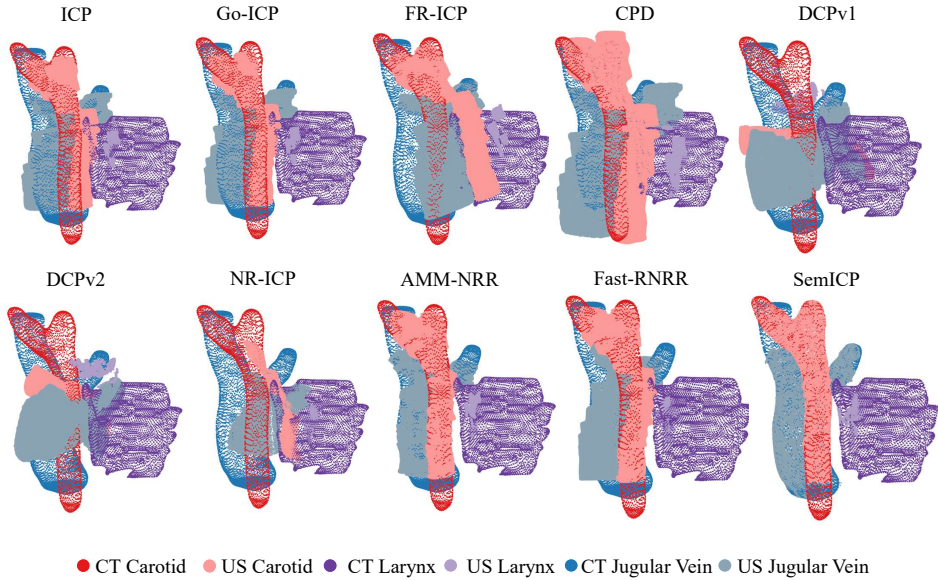


Figure 2: Visualization of the registration results on one example US-CT pair in TORS dataset (posterior-anterior view). The medial-lateral view is shown in supplemental Fig. S1.

Table 2: The average HD95 on the Learn2reg AbdominalMRCT. The metrics are reported in mean (std) in *mm* and the best performance is highlighted in bold.

	HD95					MSD					Runtime
	Liver	Spleen	Kidney-R	Kidney-L	Average	Liver	Spleen	Kidney-R	Kidney-L	Average	
Initial	38.07 ± 14.60	37.12 ± 17.25	34.41 ± 20.42	33.15 ± 14.37	35.69	18.22 ± 7.00	18.22 ± 11.84	17.05 ± 12.99	14.32 ± 6.04	16.95	
ICP	22.02 ± 7.41	15.00 ± 4.34	13.12 ± 4.91	17.25 ± 6.95	16.85	9.41 ± 3.60	6.67 ± 2.38	5.82 ± 2.38	7.08 ± 3.14	7.24	<b>0.04 ± 0.01</b>
GO-ICP	21.95 ± 7.84	14.80 ± 4.45	12.41 ± 5.03	16.74 ± 6.67	16.47	9.19 ± 3.86	6.54 ± 2.27	5.47 ± 3.47	6.99 ± 2.95	7.05	16.39 ± 20.29
FR-ICP	26.35 ± 10.78	24.29 ± 11.60	14.59 ± 7.86	22.70 ± 10.06	21.98	9.07 ± 3.82	9.65 ± 5.52	5.64 ± 2.66	8.69 ± 4.46	8.26	155.87 ± 60.02
CPD	20.53 ± 9.73	24.19 ± 18.81	11.93 ± 4.96	11.00 ± 4.91	16.91	8.53 ± 3.28	11.06 ± 9.33	5.09 ± 1.64	4.32 ± 1.29	7.25	2.82 ± 0.52
DCPv1	59.76 ± 14.24	88.37 ± 34.20	71.61 ± 15.10	66.82 ± 30.57	71.64	21.74 ± 3.94	55.94 ± 29.14	39.57 ± 12.73	33.34 ± 18.90	37.65	0.83 ± 1.86
DCPv2	62.70 ± 26.93	126.96 ± 60.90	98.70 ± 48.30	81.23 ± 41.01	92.40	25.97 ± 10.92	91.49 ± 61.39	65.54 ± 39.96	51.57 ± 34.15	58.65	0.83 ± 1.86
nr-ICP	5.80 ± 6.20	5.14 ± 6.33	6.56 ± 8.28	10.15 ± 11.01	6.91	2.45 ± 2.72	2.15 ± 2.47	2.71 ± 3.52	4.04 ± 4.62	2.84	543.08 ± 336.46
AMM-NRR	6.05 ± 2.25	6.87 ± 4.58	22.20 ± 27.03	17.71 ± 17.01	13.21	2.00 ± 0.69	2.33 ± 1.35	10.88 ± 17.96	4.84 ± 4.16	5.01	664.61 ± 211.11
Fast-RNRR	16.95 ± 17.57	10.45 ± 13.59	18.55 ± 20.74	12.68 ± 12.85	14.66	6.86 ± 8.61	4.71 ± 6.83	9.26 ± 12.39	5.01 ± 5.80	6.46	367.09 ± 168.03
SemICP	<b>1.15 ± 0.16</b>	<b>1.05 ± 0.05</b>	<b>1.23 ± 0.27</b>	<b>1.29 ± 0.28</b>	<b>1.18</b>	<b>0.68 ± 0.08</b>	<b>0.63 ± 0.03</b>	<b>0.70 ± 0.09</b>	<b>0.72 ± 0.06</b>	<b>0.68</b>	33.68 ± 14.30

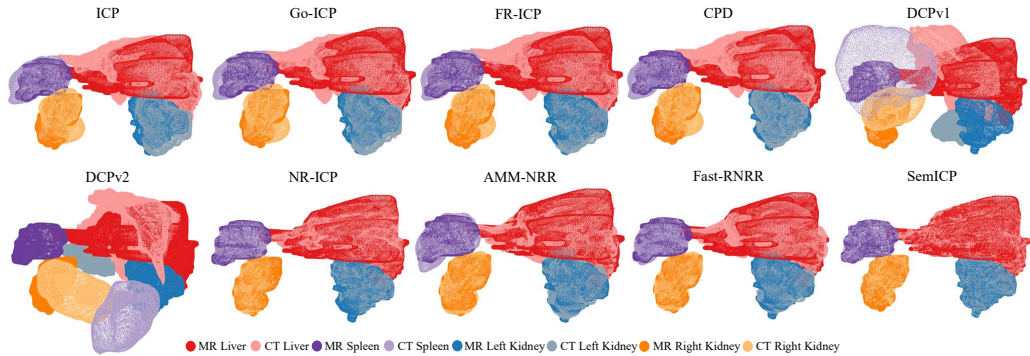


Figure 3: Visualization of the registration results on one example CT-MR pair in the AbdominalMRCT dataset (posterior-anterior view). Another viewpoint showing the left-to-right perspective is shown in the supplemental material Fig. S2.

challenge of this dataset is that the organs undergo significant deformation, so all rigid registration methods have a relatively large surface distance as shown in Fig. 3. DCP models achieve the lowest registration accuracy due to the domain mismatch, and it is worth noting that it will be hard to train a model since we have only 8 pairs of data. Our method achieves the lowest surface distance for all organs compared to baseline methods, and the registration time is approximately 33 seconds, which is acceptable for intraoperative systems.

**HippocampusMR:** HD95 and MSD results are reported in Table 3, and the qualitative results are shown in Fig. 4. This dataset includes only the head and tail of the hippocampus, which are relatively small structures with limited deformation compared to abdominal organs. While other non-rigid methods also achieve sub-millimeter MSD, and nr-ICP also achieves sub-millimeter HD95, our method SemICP yields the lowest distance errors.

Table 3: The average HD95 on the Learn2reg hippocampusMR. The metrics are reported in mean (std) in *mm*.

	HD95			MSD			Runtime
	Head	Tail	Average	Head	Tail	Average	
Initial	$3.68 \pm 1.46$	$3.68 \pm 1.23$	3.68	$1.73 \pm 0.73$	$1.60 \pm 0.48$	1.67	
ICP	$2.40 \pm 0.96$	$2.19 \pm 0.91$	2.30	$1.04 \pm 0.35$	$0.93 \pm 0.28$	0.99	<b><math>0.03 \pm 0.00</math></b>
GO-ICP	$2.46 \pm 1.04$	$2.23 \pm 1.12$	2.32	$1.03 \pm 0.37$	$0.94 \pm 0.32$	0.98	$7.60 \pm 2.74$
FR-ICP	$2.84 \pm 1.43$	$2.46 \pm 1.29$	2.64	$1.09 \pm 0.47$	$0.91 \pm 0.31$	1.00	$3.46 \pm 1.01$
CPD	$2.17 \pm 0.78$	$2.22 \pm 0.97$	2.19	$0.94 \pm 0.24$	$0.92 \pm 0.26$	0.93	$3.40 \pm 0.41$
DCPv1	$10.33 \pm 6.22$	$10.99 \pm 5.34$	10.66	$5.36 \pm 4.14$	$4.69 \pm 2.48$	5.03	$0.07 \pm 0.25$
DCPv2	$12.60 \pm 6.02$	$13.47 \pm 5.41$	13.03	$6.81 \pm 4.16$	$5.88 \pm 2.67$	6.35	$0.08 \pm 0.26$
nr-ICP	$0.77 \pm 0.37$	$0.79 \pm 0.56$	0.78	$0.38 \pm 0.11$	$0.38 \pm 0.13$	0.38	$9.97 \pm 2.70$
AMM-NRR	$2.61 \pm 1.60$	$2.12 \pm 1.45$	2.36	$0.95 \pm 0.50$	$0.76 \pm 0.31$	0.85	$10.73 \pm 2.51$
Fast-RNRR	$1.57 \pm 1.26$	$1.29 \pm 1.13$	1.43	$0.62 \pm 0.38$	$0.52 \pm 0.24$	0.57	$6.93 \pm 1.31$
SemiICP	<b><math>0.36 \pm 0.03</math></b>	<b><math>0.36 \pm 0.02</math></b>	<b>0.36</b>	<b><math>0.17 \pm 0.01</math></b>	<b><math>0.17 \pm 0.01</math></b>	<b>0.17</b>	$4.65 \pm 0.61$

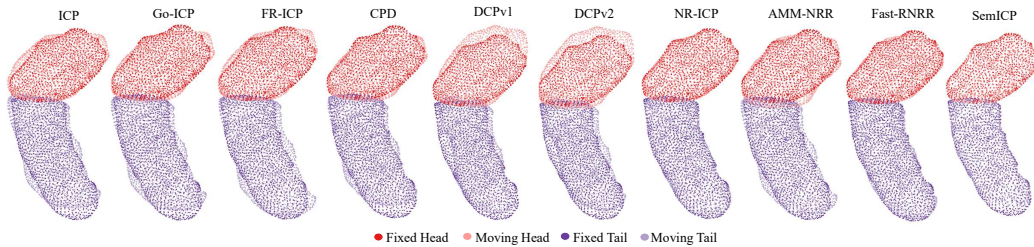


Figure 4: Visualization of the registration results on one example MR-MR pair in HippocampusMR dataset (superior-inferior view). Another viewpoint showing the left-to-right perspective is shown in the supplemental material Fig. S3.

AMM-NRR and Fast-RNRR completed registration on 58 pairs, with two pairs excluded due to numerical issues while building the deformation graph and sampling the influencing node sets.

### 3.5. Integration with Learned Labels

We use the Liver MR-3D US dataset to perform a proof-of-concept integration with learned labels. We perform a five-fold cross-validation on the segmentation-registration integration pipeline. These data are accompanied by liver US elastography and magnetic resonance elastography to evaluate liver stiffness, and the measurement of liver stiffness ranges from 5kPa to 16kPa (Zeng et al. (2024)). Therefore, we choose to set  $E$  as 10kPa. We uniformly sampled  $25 \times 25 \times 25$  control points in the  $[-1, 1]^3$  space, and the resulting spacing of the control grids is 9.99 mm  $\times$  6.78 mm  $\times$  7.19 mm.

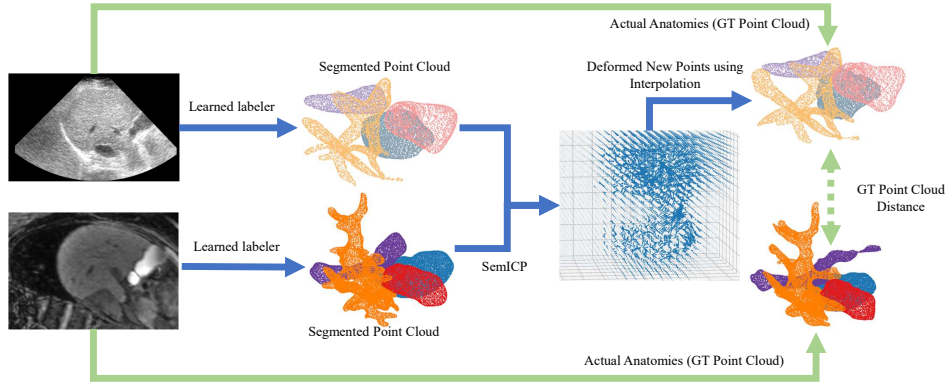


Figure 5: The proof-of-concept integration with learned labels study.

We use nnUNet (Isensee et al. (2021)) as the semantic labeler, since it achieves compatible or superior performance with other state-of-the-art semantic segmentation models on different datasets (Isensee et al. (2024)). After trained nnUNet segments the MR and US volumes, we use the segmented point clouds to register the US point cloud to the MR point cloud using semiICP. The goal of the experiment is to show that with easy-to-use segmentation models, our method can register the segmented point clouds that are not as perfect as the ground truth point clouds, instead of focusing on improving the point cloud segmentation quality. More advanced segmentation models may achieve better point cloud segmentation and further improve the registration. Moreover, we use the estimated deformation to warp the US point clouds labeled by an experienced researcher (ground truth point clouds), and evaluate the surface distance between the deformed ground truth US point clouds and the ground truth MR point clouds. This experiment demonstrates that, with our novel deformation representation, the estimated deformation can be readily transferred to new point cloud pairs, a capability that conventional point-matching-based registration methods do not provide. The experiment workflow is shown in Fig. 5.

The results of nnUNet segmentation are shown in Table 4, showing that the segmented point clouds are not perfectly accurate. The Dice coefficient is higher for MRI images but lower for US due to the lower image quality and higher noise-to-signal ratio in US. Using the segmented point clouds for registration, the corresponding results are shown in Table 5, and the quali-

Table 4: nnUnet learning based segmentation 5-fold evaluation results (Seg vs GT) with Dice and IoU. The metrics are reported in mean (std). MR results are reported on the top two rows, followed by US results at the bottom.

Dataset	Metrics	Gallbladder	IVC	Right Kidney	Vessels	Average
<b>MR T1-W</b>	Dice	0.867(0.073)	0.773(0.095)	0.955(0.010)	0.729(0.085)	0.831(0.066)
	IoU	0.762(0.088)	0.630(0.106)	0.918(0.012)	0.578(0.096)	0.722(0.075)
<b>US Bmode</b>	Dice	0.771(0.069)	0.700(0.076)	0.606(0.091)	0.689(0.073)	0.692(0.072)
	IoU	0.670(0.075)	0.560(0.081)	0.520(0.102)	0.543(0.084)	0.573(0.082)

Table 5: The average HD95 on the liver MR-3D US registration. The metrics are reported in mean (std) in *mm*. Seg refers to the evaluation of the point clouds labeled by learning-based models, and GT refers to the results on the ground truth point clouds.

		Initial		SemICP-rigid		SemICP-final	
		HD95	MSD	HD95	MSD	HD95	MSD
Gallbladder	Seg	11.21 ± 12.15	5.20 ± 8.92	8.92 ± 7.21	3.96 ± 4.46	1.07 ± 0.12	0.58 ± 0.06
	GT	9.42 ± 3.89	4.19 ± 1.90	8.86 ± 4.49	3.99 ± 2.68	5.06 ± 3.06	2.21 ± 1.77
IVC	Seg	11.07 ± 6.60	4.54 ± 2.73	9.77 ± 8.15	4.16 ± 3.63	1.36 ± 1.17	0.65 ± 0.20
	GT	11.39 ± 7.42	4.78 ± 3.41	11.48 ± 10.52	4.77 ± 4.30	7.87 ± 7.54	2.85 ± 2.39
Kidney	Seg	21.97 ± 25.26	12.14 ± 24.16	16.60 ± 12.94	7.38 ± 11.86	1.17 ± 0.37	0.61 ± 0.14
	GT	15.63 ± 5.17	7.13 ± 4.71	13.99 ± 3.23	5.32 ± 2.24	6.41 ± 4.62	2.49 ± 1.85
Liver vessel	Seg	7.82 ± 5.00	2.96 ± 1.53	9.16 ± 6.98	3.68 ± 2.93	1.58 ± 0.37	0.74 ± 0.10
	GT	9.92 ± 4.97	3.52 ± 1.58	11.51 ± 7.17	4.37 ± 3.09	8.61 ± 5.44	2.59 ± 1.53
Time				7.64 ± 1.12		14.37 ± 5.28	

tative example for one MR-US pair is shown in Fig. 6. We first observe that SemICP improves the alignment of segmented point clouds, even though they are not perfectly labeled. Moreover, the results show that the deformation estimated through learning-based labeling and registration also enhances the alignment of the ground-truth point clouds. These findings demonstrate that our proposed method can effectively handle imperfect segmentations and still achieve accurate MR-US alignment.

### 3.6. Ablation Studies

We perform two different experiments to evaluate the effect of label consistency constraints and elastic energy regularization. The experiments are performed on the AbdominalMRCT dataset. We switch off the label consistency constraints in SemICP while keeping the regularizations (W/o semantic matching + *Reg*). In the point matching step, the points from the source point cloud will be matched to the closest points in the target point cloud,

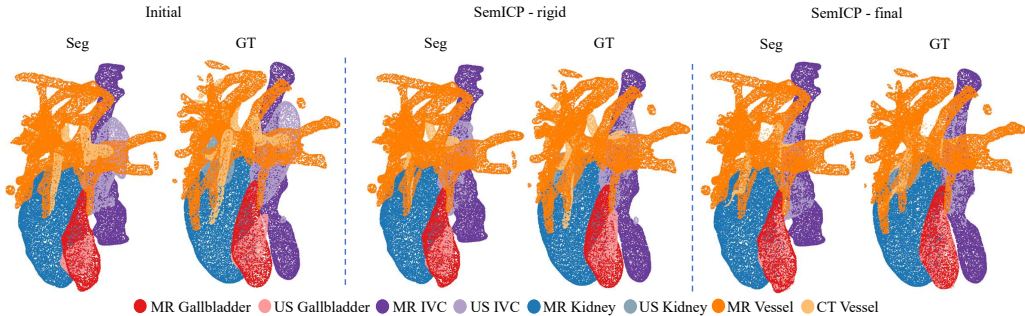


Figure 6: Visualization of the liver case study integrating with learned labelers (anterior-posterior view). Another viewpoint showing the left-to-right perspective is shown in the supplemental material Fig. S4.

without requiring that the label of the points be consistent. We also evaluate the proposed elastic energy regularization by performing SemICP with different combinations of the regularization terms.

The results of these two experiments are shown in Table 6. Comparing W/o semantic matching +  $Reg$  and Semantic +  $Reg$ , both HD95 and MSD are improved with semantic-informed matching. As shown in Fig. 7(a), the absence of semantic consistency leads SemICP to predict anatomically implausible boundaries due to organ mismatches. Table 6 also shows that the deformation field without any regularization (Semantic w/o  $Reg$ ) has the highest SDLogJ, indicating significant distortion. Among the individual regularization terms (Semantic +  $Reg_{grad}$ , Semantic +  $Reg_{mag}$ , Semantic +  $Reg_{els}$ ), Semantic +  $Reg_{els}$  achieves the lowest SDLogJ while maintaining comparable HD95 and MSD. This suggests that  $Reg_{els}$  best preserves deformation topology without sacrificing surface distance accuracy. It also outperforms  $Reg_{grad}$  in maintaining deformation smoothness. Fig. 7(b) also shows that our regularization generates a smoother deformation map.

### 3.7. Sensitivity on Elasticity Values

To evaluate the sensitivity of our method to the Young’s modulus  $E$  and Poission’s ratio  $\nu$ , we perform SemICP on the AbdominalMRCT dataset with varying elastic values. Based on finite element simulation (Brock et al. (2005)), typical  $E$  for soft tissues and abdominal organs ranges from 1kPa to 100 kPa, except only the stomach which reaches 500kPa, and  $\nu$  typically ranges from 0.400 to 0.499. In  $E$  sensitivity analysis, we fixed  $\nu = 0.499$  and

Table 6: Ablation studies on with semantic-informed matching and regularization terms. HD95 and MSD are reported in *mm*. The best values are bold and the second best is underlined. \* means the the results is significant difference compared with Semantic + *Reg* under  $p \leq 0.05$  in a two-sample t-test.

	HD95 ↓	MSD ↓	SDLogJ ↓
Initial	35.69	16.95	N/A
W/o semantic matching + <i>Reg</i>	2.42*	0.90*	0.0074
Semantic w/o <i>Reg</i>	<b>1.15*</b>	<b>0.66*</b>	0.3735*
Semantic + <i>Reg<sub>grad</sub></i>	<b>1.15*</b>	<b>0.66*</b>	0.0137*
Semantic + <i>Reg<sub>mag</sub></i>	<b>1.15*</b>	<b>0.66*</b>	0.0259*
Semantic + <i>Reg<sub>els</sub></i>	<u>1.17</u>	<u>0.67</u>	0.0074
Semantic + <i>Reg<sub>grad</sub></i> + <i>Reg<sub>mag</sub></i>	<b>1.15*</b>	<b>0.66*</b>	0.0134*
Semantic + <i>Reg<sub>grad</sub></i> + <i>Reg<sub>els</sub></i>	<u>1.17</u>	<u>0.67</u>	<u>0.0073</u>
Semantic + <i>Reg<sub>mag</sub></i> + <i>Reg<sub>els</sub></i>	<b>1.15</b>	<u>0.67</u>	0.0074
Semantic + <i>Reg</i> (Ours)	<u>1.17</u>	<u>0.67</u>	<b>0.0072</b>

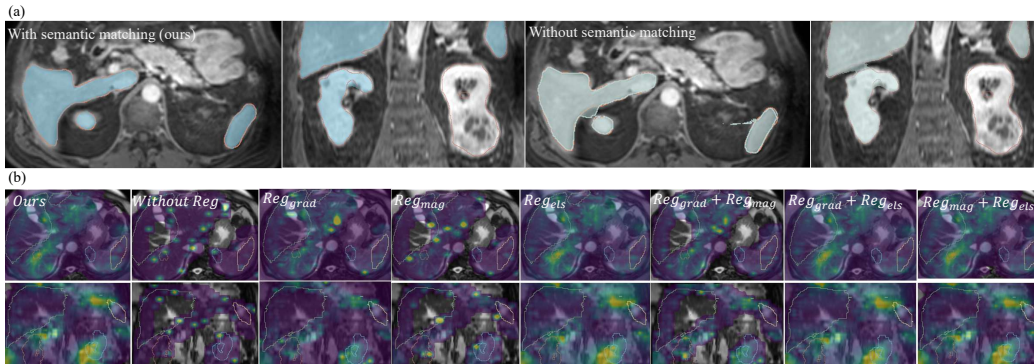


Figure 7: (a) Comparison of SemICP with and without semantic matching. Left: With semantic+*Reg* (axial and coronal views); Right: Without semantic+*Reg* (axial and coronal views). The red contour shows the MR segmentation boundary, and the colored mask represents the registered CT. (b) Comparison of deformation fields under different regularization terms. Yellow indicates larger deformation amplitude; contours represent the MR organ segmentation. The elastic regularization achieves a smoother change of the amplitude in the deformation field compared with gradient or magnitude regularization. (Top row: axial view; bottom row: coronal view.)

Table 7: The average HD95, MSD and SDLogJ of all labels for different Young’s Modulus  $E$ , while  $\nu = 0.499$ . HD95 and MSD are reported in  $mm$ . \* means the results are significantly different compared with  $E=1kPa$  under  $p \leq 0.05$  in a two-sample t-test.

$E$	1kPa	10kPa	100kPa	500kPa	1MPa
HD95 ↓	1.17	1.20*	1.23*	1.49	1.85*
MSD ↓	0.67	0.68*	0.71*	0.81	0.91*
SDLogJ ↓	0.0074	0.0053*	0.0034*	0.0024*	0.0022*

Table 8: The average HD95, MSD and SDLogJ of all labels for different Poisson’s ratio  $\nu$ , with  $E=1kPa$ . HD95 and MSD are reported in  $mm$ . \* means the results are significantly different compared with  $\nu = 0.499$  under  $p \leq 0.05$  in a two-sample t-test.

$\nu$	0.350	0.400	0.450	0.499
HD95 ↓	1.16*	1.16	1.16*	1.17
MSD ↓	0.66*	0.66*	0.66*	0.67
SDLogJ ↓	0.0117*	0.0114*	0.0112*	0.0074

varied  $E$  across {1kPa, 10kPa, 100kPa, 500kPa, 1MPa}. To also understand the influence of  $\nu$ , we fixed  $E$  at 1kPa and varied  $\nu$  in {0.350, 0.400, 0.450, 0.499}.

The sensitivity to Young’s modulus  $E$  is presented in Table 7. As  $E$  increases, the surface matching errors HD95 and MSD increase slightly, while the spatial distortion SDLogJ decreases. However, the absolute differences across metrics remain small, particularly between 1kPa and 100kPa. The results indicate that as the tissue stiffness increases, the estimated deformation becomes more regularized, but its ability to accurately fit the boundary conditions slightly diminishes. However, in the soft tissues and soft organs range, the differences in performance are small. The sensitivity to Poisson’s Ratio  $\nu$  is shown in Table 8. The surface matching has a slight improvement when the  $\nu$  decreases, while the SDLogJ increases. It indicates that assuming greater tissue compressibility weakens the linear energy regularization, allowing larger but less regularized deformations to fit the boundary conditions. Nonetheless, the differences in metrics remain small.

### 3.8. Sensitivity on Misalignment and Visualizable Ratio

To assess the sensitivity of our method and its robustness with respect to initial misalignments, we simulated partial observations and applied dif-

ferent rigid misalignments to the AbdominalMRCT dataset. We cropped the original point clouds to partially visible point clouds with 5%, 10%, 25% and 50% of points visible, and introduced additional Gaussian noise. We also added different levels of misalignment, with Euler rotation angles within  $\pm 5^\circ$ ,  $\pm 15^\circ$ , and  $\pm 30^\circ$ . For each experiment, we generated 10 different simulated partial point clouds for each patient, resulting in a total of 80 synthetic point cloud pairs. We compare our SemICP-rigid method with ICP and its variants to show how the semantic matching improves ICP robustness. FR-ICP is excluded from comparison due to its higher HD95 in Table 2, indicating less favorable performance. Therefore, we limited the comparison to ICP and GO-ICP. The point clouds are not downsampled before running ICP, GO-ICP or semICP-rigid in this experiment.

As shown in Table 9, SemICP-rigid achieves lower HD95, MSD, and TRE compared to ICP and GO-ICP under challenging visibility conditions (5%, 10%, and 25%). When evaluating sensitivity to initial misalignment, both ICP and GO-ICP exhibit significantly increased registration error at rotation angles of  $\pm 30^\circ$ , indicating sensitivity to initialization. In contrast, SemICP-rigid demonstrates improved robustness, with smaller error increases under the same conditions. These results highlight that incorporating semantic labels enhances the accuracy and stability of the rigid registration step, even under limited visibility and challenging initial alignment.

#### 4. Discussion

The datasets in our evaluation present different challenges. The TORS dataset features partial point cloud registration and suffers from severe class imbalance, making consistent registration difficult. AbdominalMRCT has large displacements between point clouds. HippocampusMR, on the other hand, features small structures, requiring precise, fine-scale registration. Our method improves the delineation of anatomical structures and consistently achieves lower HD95 and MSD values compared to existing approaches, highlighting the strength of our proposed method. Our non-rigid registration method, which crucially involves the use of semantic labeling in point matching, greatly improved registration accuracy. Label-informed matching effectively reduces mismatches that are commonly encountered in traditional point-matching-based methods, and the ablation study demonstrates that without semantic matching in SemICP, the HD95 and MSD increase. Overall, our findings show that incorporating semantic context into the regis-

Table 9: The average HD95, MSD and TRE of all labels for different rigid ICP methods with variant visible ratios of the point cloud. The numbers are reported in *mm*. The best values are bold and the second best is underlined. \* means the results are significantly different compared with the best or the second-best experiments under  $p \leq 0.05$  in a two-sample t-test.

Vis	Rot	Init			ICP			GO-ICP			SemICP-rigid		
		HD95	MSD	TRE	HD95	MSD	TRE	HD95	MSD	TRE	HD95	MSD	TRE
5%	$\pm 5^\circ$	13.60	6.31	14.17	43.31	29.53	59.28	<u>9.39</u>	<u>4.02</u>	<u>8.58</u>	<b>9.24*</b>	<b>3.94</b>	<b>8.23</b>
	$\pm 15^\circ$	32.95	19.52	42.73	36.20	23.70	51.99	<u>12.09</u>	<u>5.85</u>	<u>14.20</u>	<b>10.12*</b>	<b>4.34*</b>	<b>10.42*</b>
	$\pm 30^\circ$	61.06	43.25	80.26	42.35	28.89	61.36	<u>27.97</u>	<u>18.15</u>	<u>40.61</u>	<b>13.82*</b>	<b>6.27*</b>	<b>19.75*</b>
10%	$\pm 5^\circ$	13.74	6.22	13.19	42.49	28.24	55.73	<u>9.27</u>	<u>3.96</u>	<u>8.35</u>	<b>9.23</b>	<b>3.95</b>	<b>8.20</b>
	$\pm 15^\circ$	30.90	17.45	38.22	35.83	23.23	47.19	<u>11.34</u>	<u>5.20</u>	<u>12.32</u>	<b>10.19</b>	<b>4.41</b>	<b>10.10</b>
	$\pm 30^\circ$	55.44	35.60	70.28	36.21	22.75	50.35	<u>23.59</u>	<u>13.28</u>	<u>32.00</u>	<b>14.55*</b>	<b>6.44*</b>	<b>18.55*</b>
25%	$\pm 5^\circ$	13.73	6.09	14.11	17.62	9.49	20.22	<u>9.38</u>	<u>3.98</u>	<u>8.30</u>	<b>9.37*</b>	<b>3.97*</b>	<b>8.22*</b>
	$\pm 15^\circ$	33.27	17.21	40.83	18.84	9.58	22.65	<u>10.53</u>	<u>4.48</u>	<u>10.16</u>	<b>10.43</b>	<b>4.42</b>	<b>9.90</b>
	$\pm 30^\circ$	65.49	41.65	78.72	18.43	<u>8.52</u>	23.26	<u>16.81</u>	8.88	<u>19.40</u>	<b>15.41</b>	<b>6.74*</b>	<b>17.79</b>
50%	$\pm 5^\circ$	14.92	6.49	14.99	9.77	4.13	8.62	<u>9.55</u>	<u>4.03</u>	<u>8.34</u>	<b>9.54</b>	<b>4.03</b>	<b>8.31*</b>
	$\pm 15^\circ$	33.74	16.19	38.32	11.16	4.70	10.26	<b>10.82</b>	<b>4.54</b>	<b>9.78</b>	<u>10.91*</u>	<u>4.58*</u>	<u>9.88</u>
	$\pm 30^\circ$	72.80	43.07	81.74	<u>14.02</u>	<u>5.84</u>	<u>13.89</u>	<b>13.16</b>	<b>5.42</b>	<b>12.29</b>	16.70*	7.10*	18.05*

tration pipeline substantially improves accuracy and anatomical plausibility across a wide range of scenarios. The sensitivity study further demonstrates that the semantic context can improve the rigid initialization in challenging scenarios, including low visibility and large initial misalignment.

Our work introduces a novel biomechanical energy-based regularization into point-matching-based point cloud registration. Existing methods (NR-ICP, AMM-NRR and Fast-RNRR) regularize the deformation with a local affine regularization to constrain deformation, which fails to capture the underlying biomechanical properties of medical point clouds. Moreover, these methods focus solely on surface matching, neglecting the fact that medical point clouds often undergo deformation as cohesive volumetric structures. This limits their ability to assess and preserve the underlying deformation topology. Our elastic energy-based regularization is physically motivated by the biomechanical properties of anatomical structures, and the ablation studies confirm that the inclusion of the proposed elastic energy regularization leads to significant improvements in the plausibility and quality of the estimated deformation fields, as evidenced by reduced SDLogJ, with little degradation in the surface matching accuracy.

We do not apply the actual elasticity values in the regularization, but the sensitivity studies show that the differences in HD95, MSD and SDLogJ remain small with various  $E$  and  $\nu$ . The non-rigid cost function includes two

parts: the first part is boundary conditions that drive the alignment of the organ surfaces, and the second part is the regularization that includes elastic energy. They work together to reach the equilibrium between accuracy and smoothness. Our sensitivity experiments on  $E$  show that the registration is more likely to be driven by boundary conditions than by the regularization, particularly when  $E$  is within the range of 1kPa to 100kPa, including the soft organs of interest like liver and kidney (Kruse et al. (2000)) and brain (Murphy et al. (2019)). Similar results are observed in finite element-based registration. Chi et al. (2006) found that a 30% material uncertainty results in registration errors within 1.3mm for thin and hollow structures, and though the maximum error for prostate can reach up to 4.5mm, most of the subvolumes have a much smaller registration error. Our sensitivity experiments on  $\nu$  indicate that  $\nu$  has a small influence on the registration results, which is similar to the finding in the finite element-based registration (Brock et al. (2005)) that varying  $\nu$  only leads to small changes in accuracy. In the future, inhomogeneous  $E$  and  $\nu$  can be employed based on the labels or information from elastography (Nir et al. (2013)). More complicated non-linear effects might be integrated, but it requires the consideration of the trade-off between algorithm complexity and accuracy. A research in finite element-based lung registration shows that the registration error is not significantly affected by the element type (elastic and hyperelastic) or linearity of analysis, suggesting the use of linear finite element analysis for simplicity (Al-Mayah et al. (2011)).

In our experiments, AMM-NRR and Fast-RNRR encountered numerical problems during the initialization phase of non-rigid registration on several samples. These issues arose during the construction of the deformation graph, where small and irregular triangle faces resulted in unstable edge angle computations. This sensitivity to mesh quality highlights a limitation of their approach: it relies on geometric assumptions that do not generalize well to real-world medical data, which often contains non-uniform, sparse, or noisy point distributions. As a result, their methods may fail or produce unreliable deformations when applied to anatomically complex point clouds, limiting their robustness in clinical scenarios.

The deep learning-based methods, DCPv1 and DCPv2, increase the surface alignment error in the datasets. The results demonstrate that models trained on daily object data can not be utilized in the medical point clouds in an out-of-the-box manner, which is consistent with findings in previous works (Weber et al. (2024); Zhang et al. (2024)). It is possible that the ModelNet40

data of daily objects typically include clear feature points, such as corners and lines, to assist the alignment, while the medical surfaces typically exhibit smoother local curvature and can be partially visible. As a result, models trained on regular objects such as ModelNet40 can not learn the features that generalize well to medical data. Our non-learning, semantic-aware registration framework circumvents this limitation by directly leveraging anatomical labels and biomechanical constraints without relying on large-scale, object-domain pretraining.

Our work requires semantic labels in the point cloud, and this paper focuses on registration and does not address the segmentation process in detail. We present a proof-of-concept study of integrating a deep learning model to segment the volumes from different modalities and to perform the registration on the imperfectly segmented point clouds. Our experiments show that our method can register the less ideal point clouds, supporting its feasibility for integration into US-based image guidance systems, where segmentation and registration must operate on noisy or incomplete data. Moreover, we highlight that our control-grid-based deformation enables warping the ground truth point cloud labeled by human experts. It is almost impossible to transfer the registration results from the segmented point cloud pairs to ground truth point cloud pairs using other non-rigid point-matching-based registration, since it is difficult to interpolate the motion of points from the sparse surface point correspondences. Especially when the segmentation point clouds have mis-segmentation, the motion in the unobserved region can not be approximated easily. Our method, with an explicit deformation field, can estimate the movement of unseen points within the deformation field through interpolating their motions based on control grids. The method makes it possible to estimate the motion of new or unobserved regions, even when segmentation inaccuracies are present. This proof of concept demonstrates a possible pathway toward integrating learning-based segmentation and non-rigid point cloud registration into US-guided intervention workflows.

This method is designed for multi-organ registration, but it has the potential to be generalized to single-organ registration as long as the point clouds have different semantic labels (such as using vessels inside the liver as additional labels). Additionally, the homogeneous linear elastic energy is a simplified model, and future work can explore the use of different biomechanical parameters for different control points based on the type of tissue.

## 5. Conclusion

We present a novel non-rigid point cloud registration method that extends semantic label-based point matching to improve the quality of the matched point pairs in medical point clouds. We utilize a novel control point-based deformation representation to enable explicit biomechanics-based regularization in point cloud registration. Our method outperforms state-of-the-art point-matching-based registration methods on three different datasets, showing that it is generalizable to different tasks and challenges. Through a proof-of-concept study, we demonstrate that integrating deep learning segmentation with our registration pipeline enables effective alignment of imperfectly segmented US and MR point clouds. These results highlight the potential of our framework to be used in CAI systems.

### **CRedit authorship contribution statement**

**Wanwen Chen:** Conceptualization, Methodology, Software, Visualization, Investigation, Data curation, Formal analysis, Writing - original draft; **Qi Zeng:** Software, Formal analysis, Data curation, Investigation, Writing - review and editing; **Carson Studders:** Software, Visualization, Data curation, Writing - review and editing; **Jamie J.Y. Kwon:** Investigation, Data curation; **Emily H.T. Pang:** Investigation, Data curation, Supervision; **Eitan Prisman:** Conceptualization, Investigation, Data Curation, Funding acquisition, Supervision, Resources; **Septimiu E. Salcudean:** Conceptualization, Methodology, Funding acquisition, Supervision, Resources, Writing - review and editing.

### **Declaration of competing interest**

The authors have no competing interests to declare that are relevant to the content of this article.

### **Acknowledgment**

The work is supported by an NSERC Discovery Grant and the Charles Laszlo Chair in Biomedical Engineering held by Dr. Salcudean, and by the VCHRI Innovation and Translational Research Award, the University of British Columbia Department of Surgery Seed Grant and CIHR Project Grant held by Dr. Prisman.

## Data statement

Data from the TORS study and the liver study are not openly available due to the ethical restrictions, that the data contain sensitive patient information. Learn2reg challenge datasets are available through accessing the challenge website <https://learn2reg.grand-challenge.org/Datasets/>. Learn2reg AbdomenMRCT dataset is openly available in <https://cloud.imi.uni-luebeck.de/s/32WaSRaTnFk2JeT>. Learn2reg hippocampus dataset is openly available in <https://cloud.imi.uni-luebeck.de/s/gPN6bzJ4xf7HzG8>.

## Declaration of generative AI and AI-assisted technologies in the manuscript preparation process

Statement: During the preparation of this work, the author(s) used ChatGPT for grammar correction and language editing. After using this tool/service, the author(s) reviewed and edited the content and take(s) full responsibility for the content of the published article.

## References

- Al-Mayah, A., Moseley, J., Velec, M., Brock, K., 2011. Toward efficient biomechanical-based deformable image registration of lungs for image-guided radiotherapy. *Physics in Medicine & Biology* 56, 4701.
- Amberg, B., Romdhani, S., Vetter, T., 2007. Optimal step nonrigid icp algorithms for surface registration, in: *2007 IEEE conference on computer vision and pattern recognition (CVPR)*, IEEE. pp. 1–8.
- Bayrak, M., Alsadoon, A., Prasad, P., Venkata, H.S., Ali, R.S., Haddad, S., 2020. A novel rotation invariant and manhattan metric-based pose refinement: Augmented reality-based oral and maxillofacial surgery. *The International Journal of Medical Robotics and Computer Assisted Surgery* 16, e2077.
- Bernardini, F., Mittleman, J., Rushmeier, H., Silva, C., Taubin, G., 2002. The ball-pivoting algorithm for surface reconstruction. *IEEE transactions on visualization and computer graphics* 5, 349–359.
- Besl, P.J., McKay, N.D., 1992. Method for registration of 3-d shapes, in: *Sensor fusion IV: control paradigms and data structures*, SPIE. pp. 586–606.

- Brock, K., Sharpe, M., Dawson, L., Kim, S., Jaffray, D., 2005. Accuracy of finite element model-based multi-organ deformable image registration. *Medical physics* 32, 1647–1659.
- Broit, C., 1981. Optimal registration of deformed images. University of Pennsylvania.
- Chen, E., Novakofski, J., Jenkins, W., O'Brien, W., 1996. Young's modulus measurements of soft tissues with application to elasticity imaging. *IEEE Transactions on Ultrasonics, Ferroelectrics, and Frequency Control* 43, 191–194. doi:10.1109/58.484478.
- Chi, Y., Liang, J., Yan, D., 2006. A material sensitivity study on the accuracy of deformable organ registration using linear biomechanical models a. *Medical physics* 33, 421–433.
- Clark, K., Vendt, B., Smith, K., Freymann, J., Kirby, J., Koppel, P., Moore, S., Phillips, S., Maffitt, D., Pringle, M., Tarbox, L., Prior, F., 2013. The cancer imaging archive (tcia): maintaining and operating a public information repository. *Journal of digital imaging* 26, 1045–1057.
- Fedorov, A., Beichel, R., Kalpathy-Cramer, J., Finet, J., Fillion-Robin, J.C., Pujol, S., Bauer, C., Jennings, D., Fennessy, F., Sonka, M., Buatti, J., Aylward, S., Miller, J.V., Pieper, S., Kikinis, R., 2012. 3d slicer as an image computing platform for the quantitative imaging network. *Magnetic resonance imaging* 30, 1323–1341.
- Fischer, B., Modersitzki, J., 2004. A unified approach to fast image registration and a new curvature based registration technique. *Linear Algebra and its applications* 380, 107–124.
- Fischer, B., Modersitzki, J., 2008. Ill-posed medicine—an introduction to image registration. *Inverse problems* 24, 034008.
- Flepp, R., Nissen, L., Sigrist, B., Nieuwland, A., Cavalcanti, N., Fürnstahl, P., Dreher, T., Calvet, L., 2025. Automatic multi-view x-ray/ct registration using bone substructure contours. *International Journal of Computer Assisted Radiology and Surgery* , 1–8.
- Fu, Y., Lei, Y., Wang, T., Patel, P., Jani, A.B., Mao, H., Curran, W.J., Liu, T., Yang, X., 2021a. Biomechanically constrained non-rigid mr-trus

- prostate registration using deep learning based 3d point cloud matching. *Medical image analysis* 67, 101845.
- Fu, Y., Wang, T., Lei, Y., Patel, P., Jani, A.B., Curran, W.J., Liu, T., Yang, X., 2021b. Deformable mr-cbct prostate registration using biomechanically constrained deep learning networks. *Medical physics* 48, 253–263.
- Gatti, A.A., Khallaghi, S., 2022. Pycpd: Pure numpy implementation of the coherent point drift algorithm. *Journal of Open Source Software* 7, 4681.
- Hansen, L., Dittmer, D., Heinrich, M.P., 2019. Learning deformable point set registration with regularized dynamic graph cnns for large lung motion in copd patients, in: *International Workshop on Graph Learning in Medical Imaging*, Springer. pp. 53–61.
- Heinrich, M.P., Bigalke, A., Großbröhmer, C., Hansen, L., 2023. Chasing clouds: differentiable volumetric rasterisation of point clouds as a highly efficient and accurate loss for large-scale deformable 3d registration, in: *Proceedings of the IEEE/CVF international conference on computer vision (ICCV)*, pp. 8026–8036.
- Heinrich, M.P., Bigalke, A., Hansen, L., 2025. Fast forward: Rephrasing 3d deformable image registration through density alignment and splatting, in: *Medical Imaging with Deep Learning*.
- Hering, A., Hansen, L., Mok, T.C.W., Chung, A.C.S., Siebert, H., Häger, S., Lange, A., Kuckertz, S., Heldmann, S., Shao, W., Vesal, S., Rusu, M., Sonn, G., Estienne, T., Vakalopoulou, M., Han, L., Huang, Y., Yap, P.T., Brudfors, M., Balbastre, Y., Joutard, S., Modat, M., Lifshitz, G., Raviv, D., Lv, J., Li, Q., Jaouen, V., Visvikis, D., Fourcade, C., Rubeaux, M., Pan, W., Xu, Z., Jian, B., De Benetti, F., Wodzinski, M., Gunnarsson, N., Sjölund, J., Grzech, D., Qiu, H., Li, Z., Thorley, A., Duan, J., Großbröhmer, C., Hoopes, A., Reinertsen, I., Xiao, Y., Landman, B., Huo, Y., Murphy, K., Lessmann, N., van Ginneken, B., Dalca, A.V., Heinrich, M.P., 2022. Learn2reg: comprehensive multi-task medical image registration challenge, dataset and evaluation in the era of deep learning. *IEEE Transactions on Medical Imaging* 42, 697–712.
- Hiep, M., Heerink, W., Groen, H., Saiz, L.A., Grotenhuis, B., Beets, G., Aalbers, A., Kuhlmann, K.F., Ruers, T., 2025. Real-time intraoperative

- ultrasound registration for accurate surgical navigation in patients with pelvic malignancies. *International journal of computer assisted radiology and surgery* 20, 249–258.
- Isensee, F., Jaeger, P.F., Kohl, S.A., Petersen, J., Maier-Hein, K.H., 2021. nnu-net: a self-configuring method for deep learning-based biomedical image segmentation. *Nature methods* 18, 203–211.
- Isensee, F., Wald, T., Ulrich, C., Baumgartner, M., Roy, S., Maier-Hein, K., Jaeger, P.F., 2024. nnu-net revisited: A call for rigorous validation in 3d medical image segmentation, in: *International Conference on Medical Image Computing and Computer-Assisted Intervention*, Springer. pp. 488–498.
- Jiang, Z., Kang, Y., Bi, Y., Li, X., Li, C., Navab, N., 2025. Class-aware cartilage segmentation for autonomous us-ct registration in robotic intercostal ultrasound imaging. *IEEE Transactions on Automation Science and Engineering* 22, 4818 – 4830. doi:10.1109/TASE.2024.3411784.
- Khallaghi, S., Sánchez, C.A., Rasouljan, A., Sun, Y., Imani, F., Khojaste, A., Goksel, O., Romagnoli, C., Abdi, H., Chang, S., Mousavi, P., Fenster, A., Ward, A., Fels, S., Abolmaesumi, P., 2015. Biomechanically constrained surface registration: Application to mr-trus fusion for prostate interventions. *IEEE transactions on medical imaging* 34, 2404–2414.
- Kingma, D., Ba, J., 2014. Adam: A method for stochastic optimization. *arXiv preprint arXiv:1412.6980* .
- Kruse, S., Smith, J., Lawrence, A., Dresner, M., Manduca, A., Greenleaf, J.F., Ehman, R.L., 2000. Tissue characterization using magnetic resonance elastography: preliminary results. *Physics in Medicine & Biology* 45, 1579.
- Lasso, A., Heffter, T., Rankin, A., Pinter, C., Ungi, T., Fichtinger, G., 2014. Plus: open-source toolkit for ultrasound-guided intervention systems. *IEEE transactions on biomedical engineering* 61, 2527–2537.
- Lei, L., Zhao, B., Qi, X., Mi, R., Ye, H., Zhang, P., Wang, Q., Heng, P.A., Hu, Y., 2023. Robotic needle insertion with 2d ultrasound–3d ct fusion guidance. *IEEE Transactions on Automation Science and Engineering* 21, 6152–6164.

- Liebmann, F., von Atzigen, M., Stütz, D., Wolf, J., Zingg, L., Suter, D., Cavalcanti, N.A., Leoty, L., Esfandiari, H., Snedeker, J.G., Oswald, M.R., Pollefeys, M., Farshad, M., Fürnstahl, P., 2024. Automatic registration with continuous pose updates for marker-less surgical navigation in spine surgery. *Medical Image Analysis* 91, 103027.
- Ma, L., Huang, T., Wang, J., Liao, H., 2023. Visualization, registration and tracking techniques for augmented reality guided surgery: a review. *Physics in Medicine & Biology* 68, 04TR02.
- Ma, L., Liang, H., Han, B., Yang, S., Zhang, X., Liao, H., 2022. Augmented reality navigation with ultrasound-assisted point cloud registration for percutaneous ablation of liver tumors. *International journal of computer assisted radiology and surgery* 17, 1543–1552.
- Mekhzoum, H., Keelson, B., Scheerlinck, T., Vandemeulebroucke, J., 2024. Towards point cloud-based medical image registration for dynamic 4d-ct imaging, in: *International Workshop on Shape in Medical Imaging*, Springer. pp. 205–223.
- Murphy, M.C., Huston III, J., Ehman, R.L., 2019. Mr elastography of the brain and its application in neurological diseases. *Neuroimage* 187, 176–183.
- Nir, G., Sahebjavaher, R.S., Kozlowski, P., Chang, S.D., Sinkus, R., Goldenberg, S.L., Salcudean, S.E., 2013. Model-based registration of ex vivo and in vivo mri of the prostate using elastography. *IEEE transactions on medical imaging* 32, 1068–1080.
- Poiesi, F., Boscaini, D., 2022. Learning general and distinctive 3d local deep descriptors for point cloud registration. *IEEE Transactions on Pattern Analysis and Machine Intelligence* 45, 3979–3985.
- Ringel, M., Heiselman, J., Richey, W., Meszoely, I., Miga, M., 2023. Regularized kelvinlet functions to model linear elasticity for image-to-physical registration of the breast, in: *International Conference on Medical Image Computing and Computer-Assisted Intervention (MICCAI)*, Springer. pp. 344–353.
- Segal, A., Haehnel, D., Thrun, S., 2009. Generalized-icp., in: *Robotics: science and systems*, Seattle, WA. p. 435.

- Simpson, A.L., Antonelli, M., Bakas, S., Bilello, M., Farahani, K., Van Ginneken, B., Kopp-Schneider, A., Landman, B.A., Litjens, G., Menze, B., Ronneberger, O., Summers, R.M., Bilic, P., Christ, P.F., Do, R.K., Golub, M., Golia-Pernicka, J., Heckers, S.H., Jarnagin, W.R., McHugo, M.K., Napel, S., Vorontsov, E., Maier-Hein, L., Cardoso, M.J., 2019. A large annotated medical image dataset for the development and evaluation of segmentation algorithms. arXiv preprint arXiv:1902.09063 .
- Wang, D., Azadvar, S., Heiselman, J., Jiang, X., Miga, M., Wang, L., 2024. Libr+: Improving intraoperative liver registration by learning the residual of biomechanics-based deformable registration, in: International Conference on Medical Image Computing and Computer-Assisted Intervention (MICCAI), Springer. pp. 359–368.
- Wang, Q., Yang, Y., Wan, T., Du, S., 2020. Robust point set registration based on semantic information, in: 2020 IEEE International Conference on Systems, Man, and Cybernetics (SMC), IEEE.
- Wang, Y., Solomon, J.M., 2019. Deep closest point: Learning representations for point cloud registration, in: Proceedings of the IEEE/CVF international conference on computer vision (ICCV), pp. 3523–3532.
- Weber, M., Wild, D., Kleesiek, J., Egger, J., Gsaxner, C., 2024. Deep learning-based point cloud registration for augmented reality-guided surgery, in: 2024 IEEE International Symposium on Biomedical Imaging (ISBI), IEEE. pp. 1–5.
- Wu, Z., Song, S., Khosla, A., Yu, F., Zhang, L., Tang, X., Xiao, J., 2015. 3d shapenets: A deep representation for volumetric shapes, in: Proceedings of the IEEE conference on computer vision and pattern recognition, pp. 1912–1920.
- Yang, J., Li, H., Campbell, D., Jia, Y., 2015. Go-icp: A globally optimal solution to 3d icp point-set registration. *IEEE transactions on pattern analysis and machine intelligence* 38, 2241–2254.
- Yang, Z., Simon, R., Merrell, K., Linte, C.A., 2025. Boundary constraint-free biomechanical model-based surface matching for intraoperative liver deformation correction. *IEEE Transactions on Medical Imaging* 44, 1723–1734.

- Yao, Y., Deng, B., Xu, W., Zhang, J., 2020. Quasi-newton solver for robust non-rigid registration, in: 2020 IEEE/CVF Conference on Computer Vision and Pattern Recognition (CVPR), pp. 7597–7606.
- Yao, Y., Deng, B., Xu, W., Zhang, J., 2023. Fast and robust non-rigid registration using accelerated majorization-minimization. *IEEE Transactions on Pattern Analysis and Machine Intelligence* 45, 9681–9698.
- Zaganidis, A., Sun, L., Duckett, T., Cielniak, G., 2018. Integrating deep semantic segmentation into 3-d point cloud registration. *IEEE Robotics and automation letters* 3, 2942–2949.
- Zeng, Q., Honarvar, M., Schneider, C., Mohammad, S.K., Lobo, J., Pang, E.H.T., Lau, K.T., Hu, C., Jago, J., Erb, S.R., Rohling, R., Salcudean, S.E., 2021. Three-dimensional multi-frequency shear wave absolute vibro-elastography (3d s-wave) with a matrix array transducer: Implementation and preliminary in vivo study of the liver. *IEEE Transactions on Medical Imaging* 40, 648–660. doi:10.1109/TMI.2020.3034065.
- Zeng, Q., Mohammad, S., Aleef, T.A., Honarvar, M., Schneider, C., Pang, E.H., Jago, J., Ramji, A., Yoshida, E.M., Rohling, R., et al., 2024. Validation of volumetric multi-frequency shear wave vibro-elastography with matrix array transducer for the in vivo liver. *IEEE Transactions on Ultrasonics, Ferroelectrics, and Frequency Control* .
- Zhang, J., Yao, Y., Deng, B., 2022. Fast and robust iterative closest point. *IEEE Transactions on Pattern Analysis and Machine Intelligence* 44, 3450–3466.
- Zhang, Y., Zou, Y., Liu, P.X., 2024. Point cloud registration in laparoscopic liver surgery using keypoint correspondence registration network. *IEEE Transactions on Medical Imaging* 44, 749–760.